Results in Physics 17 (2020) 103102

Contents lists available at ScienceDirect

Results in Physics

journal homepage: www.elsevier.com/locate/rinp

Ag nanoparticles localised surface plasmon field regulated spectral characteristics of Ho^{3+}-doped phosphate-based glass-ceramic

Areej S. Alqarni[a,b,*], R. Hussin[a], S.N. Alamri[b], S.K. Ghoshal[a,*]

[a] Department of Physics & Laser Centre, Faculty of Science, Universiti Teknologi Malaysia, Johor, Malaysia
[b] Department of Physics, Faculty of Science, Taibah University, Madinah, Saudi Arabia

ARTICLE INFO

Keywords:
Holmium ion
Glass-ceramics
Ag NPs
Absorption
Stimulated emission cross-section
Non-radiative decay

ABSTRACT

The holmium ion (Ho^{3+})- activated phosphate-based glass-ceramics with silver nanoparticles (Ag NPs) inclusion were prepared using the standard melt-quenching. The samples were characterised to evaluate the effects of different Ag NPs contents on their structure, microstructure and optical properties. The XRD pattern of the as-quenched samples revealed their glass-ceramic nature. The FTIR and Raman analyses showed the modification of the glass-ceramics network structure due to the embedment of Ag NPs. The TEM and HRTEM images together with the localized surface plasmon resonance (LSPR) absorption bands of the glass-ceramics confirmed the existence of Ag NPs inside the host matrix. The complex impedance analyses of the glass-ceramics suggested the glassy phase dominance in the host network. The photoluminescence (PL) peak intensities were significantly enhanced due to the influence of Ag NPs enabled LSPR effects. The PL decay curve analysis of the glass-ceramics indicated the effect of Ag NPs mediated amplified local electric field and energy transfer from the Ag NPs to Ho^{3+}, a mechanism responsible for the optical traits improvement. The achieved branching ratio and stimulated emission cross-section of the optimum glass-ceramic for the three PL peaks were 73.88% and 46.68 $\times$ 10^{-21} cm^2 (green); 83.97% and 41.12 $\times$ 10^{-21} cm^2 (red); and 71.40% and 36.95 $\times$ 10^{-21} cm^2 (IR). Based on the obtained findings, a structural-optical correlation was established.

Introduction

The splitting of the 4f sub-shell of various rare earth ions (REIs) when doped in the appropriate host material can produce major absorption and emission lines responsible for a wide range of applications including lasers, light emitting diodes (LEDs), and amplifiers [1–3]. The stimulated emission cross-section (σ_P^E) of the REI is a significant parameter that describes its photoluminescence (PL) properties. Based on this factor, many research works have been dedicated to enhance the σ_P^E of the REIs by selecting the suitable host materials with low phonon energy, appropriate modifiers, and sensitizers (such as metal and semiconductor nanostructures) [4,5].

Among the ternary and quaternary oxide hosts, the phosphate-based systems are potential because of their high thermal expansion coefficient, low phonon energy, large intake of REIs and low glass transition temperature [6]. The combination of the phosphate and borate units was found to be prospective due to the enhanced chemical durability [7]. It has been acknowledged that the chemical durability and structural stability of the boro-phosphate glass can further be improved by adding metal oxide ions (e.g. Zn^{2+}) in the amorphous network structures [8]. It has also been argued that the interactions between the phosphate and sulfate ions can create a good environment for the intake of large number of REIs, allowing the fabrication of the miniaturized lasers with the improved features [9]. In brief, the zinc-sulfo-boro-phosphate composition is a viable host for the REIs doping.

The holmium ions (Ho^{3+}) among various REIs have been used in diverse technologies including the optical data storage systems, radars, lasers, amplifiers, sensors, and medical diagnostics [4]. They exhibit unique emissions in the ultraviolet (UV), visible (Vis), and infrared (IR) regions [10]. However, the intensities of these emissions still need to be improved to realize the lasers and nanophotonic devices [8]. Recently, a combination of the metal nanoparticles (NPs) with REIs in various host matrices has been proven to be advantageous for achieving the significant enhancement in the emission intensity of the REIs. The Ag NPs being the common plasmonic metamaterial with abundance, strong biocompatibility, high chemical stability and resistant against oxidation has been used as the sensitizing agent in many systems to amplify the REIs lasing action [11]. The localized surface plasmon resonance

* Corresponding authors at: Department of Physics, Faculty of Science, Universiti Teknologi Malaysia, Johor, Malaysia (S.K. Ghoshal). Department of Physics, Faculty of Science, Taibah University, Madinah, Saudi Arabia (A.S. Alqarni).
E-mail addresses: aqarni@taibahu.edu.sa (A.S. Alqarni), sibkrishna@utm.my (S.K. Ghoshal).

https://doi.org/10.1016/j.rinp.2020.103102
Received 10 February 2020; Received in revised form 4 April 2020; Accepted 6 April 2020
Available online 10 April 2020

(LSPR) effect of noble metal NPs has been demonstrated to be responsible for such significant enhancement of the optical properties [12].

Upon interaction with the incident radiation, the metal NPs develop strong local electric field (due to the LSPR) and transfer a part of the energy to the REIs that are position in the vicinity of NPs inside the host matrix, resulting in the enhanced photoluminescence (PL) emission intensity [13,14]. The relative permittivity between the host material and the surface of the NP (dielectric-metal interface) play a significant role to achieve an enhancement in the PL intensity through the LSPR mediation [15]. The dielectric function or the complex permittivity of the material decides such enhancement. The real part of the dielectric constant of the metal must be negative (nearly -5 at 3 eV for Ag) [16] and its magnitude must be greater than that of the dielectric host (approximately 3 at 3 eV without Ag for the proposed system) [17]. The complex permittivity has recently been proven to be a powerful tool to evaluate the microstructures through the complex impedance plot (Nyquist plots) in the low frequency region [17]. This in turn provides a better understanding of the appropriate selection of the host matrix to improve the spectral attributes of Ho^{3+}. In addition, most of the reported literatures [18–22] on the structural, optical and dielectric attributes of the glass-ceramic, glass, and ceramic systems rarely explained any correlation among them. However, by ascertaining such relationship in the REIs doped glasses or ceramics or glass-ceramics an in-depth understanding of the microscopic mechanisms can be developed.

Based on the aforementioned background, this paper evaluates the structural, optical and dielectric characteristics of the Ag NPs and Ho^{3+} co-activated zinc-sulfo-boro-phosphate glass-ceramics to define a possible correlation among them. The as-quenched samples were characterised by assorted analytical techniques. In addition, the Judd-Ofelt (J-O) theory was used to complement the experimental results. The obtained data were analysed, interpreted, discussed and compared. The present glass-ceramic compositions with improved optical properties were demonstrated to be prospective for the development of sundry efficient optoelectronic devices.

Experimental and theoretical

Samples preparation

A series of phosphate-based glass-ceramic nanocomposites of different compositions (Table 1) were prepared using the melt-quenching method. Analytical grade chemical reagents of H_3PO_4, and B_2O_3 were used as the network formers, while $ZnSO_4{\cdot}7H_2O$ and Ho_2O_3 were used as the network modifier and dopant, respectively. The AgCl (purity 99.999%, Sigma Aldrich) was used as the sensitizer. First, an appropriate amount of the constituent raw materials (called the batch material) were weighed using a digital balance and well mixed to assure the homogeneity. Second, an alumina crucible containing this batch was placed inside an electrical furnace (30 min at 300 °C). Next, the mixture was transferred to another furnace (90 min at 1300 °C) to complete the melting process. Then, the melt was poured onto a preheated stainless-steel plate in another furnace for further annealing (120 min at 300 °C). Last, the frozen sample was left inside the annealing furnace (turned off) to cool down naturally to the room temperature. The as-quenched sample was stored at room temperature in a humidity free environment. Same procedure was followed to synthesise all the six nanocomposites. One sample was prepared without holmium (with Ag NPs, coded as GCA0.5) and another without Ag NPs (with holmium coded as HGCA0.0). The rest of the 4 nanocomposites with the molar formula $(39.5–x)P_2O_5 – 30B_2O_3 – 30ZnSO_4 – 0.5Ho_2O_3 – xAgCl$ contained fixed amount of holmium (0.5 mol%) and varying contents of Ag NPs (x = 0.6, 0.7, 0.8 and 0.9 mol%).

Table 1
The sample code, composition, density and molar volume.

Sample code	Composition (mol%)					ρ (g cm^{-3})	V_m (cm^3 mol^{-1})
	$ZnSO_4$	B_2O_3	P_2O_5	Ho_2O_3	AgCl		
HGCA0.0	30	30	39.5	0.5	0.0	2.855	–
HGCA0.6	30	30	38.9	0.5	0.6	2.906	56.83
HGCA0.7	30	30	38.8	0.5	0.7	2.848	57.97
HGCA0.8	30	30	38.7	0.5	0.8	2.854	57.86
HGCA0.9	30	30	38.6	0.5	0.9	2.896	57.01
GCA0.5	30	30	39.5	0.0	0.5	–	–

Characterizations

The densities of the prepared glass-ceramic nanocomposites were measured using the Archimedes method where toluene served as the immersion liquid. The Shimadzu 6100 X-ray diffractometer was used for the X-ray diffraction (XRD) measurement with a step size of 0.02 in the 2θ range from 10 to 80°. The Horiba Raman spectroscopy (XploRA PLUS) in the range of 200–1600 cm^{-1} was utilised to record the Raman spectra. The Fourier transform infrared (FTIR) spectrum of the studied samples in the range of 600–1650 cm^{-1} were obtained using a Perkin-Elmer 1710 spectroscopy with ± 0.4 cm^{-1} resolution and 10 scans. The morphology and EDX maps of the prepared samples were recorded via a high-resolution transmission electron microscope (HRTEM, Jeol-ARM200F) operated at 200 kV. The HRTEM images were analysed by Gatan digital micrograph software. The transmittance and diffuse reflectance data of the samples were obtained by a Shimadzu 3600 Plus UV–Vis-NIR spectroscopy. The photoluminescence (PL) emission spectra of the samples were recorded using a Horiba-Fluoro Max-4 spectroscopy under the excitation wavelength of 450 nm. The GW INSTEK LCR-8105 G impedance spectroscopy (IS) in the range of 1-100 kHz was used to record the complex impedance data (X-R series circuit with 100 mV AC-amplitude). For the impedance measurement, the as-prepared sample was ground and compacted into a cylinder-shaped pellet (thickness: 3 mm; diameter: 13 mm) using a hydraulic press followed by the densification via annealing process (120 min at 300 °C). A gold layer was deposited on both sides of the pellet for approximately 3 min (deposition time) using the MTI corporation–plasma sputtering coater. Then, the pellet was placed between two identical copper electrodes for the measurement. All structural, optical and dielectric characterizations of the obtained nanocomposites were made at room temperature.

Results and discussion

Structure and microstructure

XRD, Raman and FTIR analyses

Fig. 1 depicts the XRD patterns of the as-quenched samples, where the occurrence of a hump in the smaller angular region accompanied by a sharp peak at 27.84° was due to the reflection from the (3 1 0) lattice plane of B_2O_3 (based on ICDD card number 000060297), confirming the formation of the glass-ceramic phase. Similar XRD peak was also reported in other boro-phosphate compositions [23–25].

Figs. 2 and 3 present the Raman and FTIR spectra of the prepared nanocomposites. The observed band positions of HGCA0.0 nanocomposite (the black profile) were explained in a recent communication [17], confirming the presence of SO_4^{2-}, BO_3, BO_4, PO_4^{3-}, Zn-O, P-O-P, B-O-P, and B_2O_3 functional groups inside the glass-ceramic nanocomposite matrix. The vibrations of the crystallite domains inside the glass-ceramic network was remarkably affected due to the incorporation of Ag NPs. In addition, the obtained spectra were well matched with the B_2O_3 Raman spectra (ROD card number 3500222) and B_2O_3 FTIR spectra for the HGCA0.7 and HGCA0.8 nanocomposites.

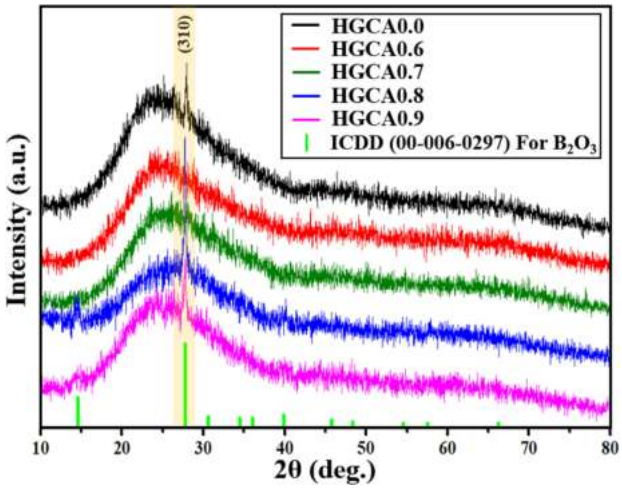

Fig. 1. The XRD patterns of the prepared samples.

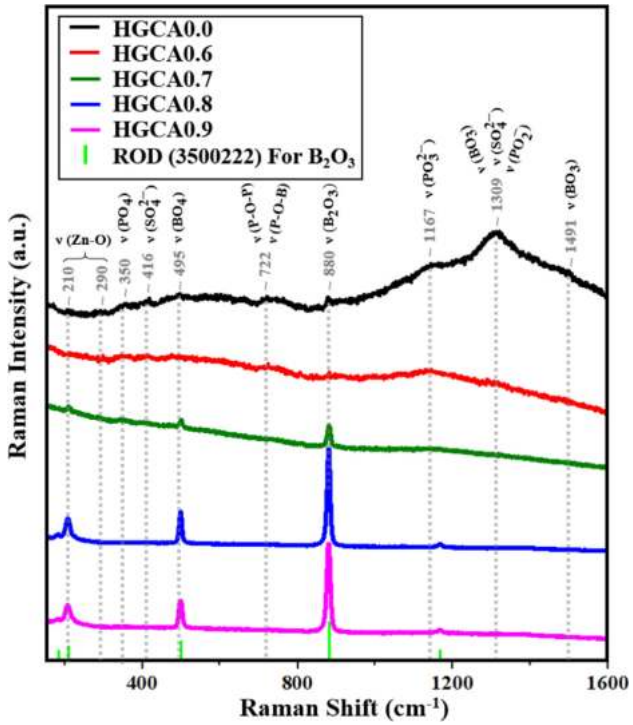

Fig. 2. The Raman spectra of the proposed glass-ceramic nanocomposites.

TEM, HRTEM and EDX analyses

Fig. 4-a shows the low magnification TEM images of the GCA0.5 nanocomposite prepared without Ho_2O_3 to detect the nucleation of Ag NPs inside the glass-ceramic network. The histogram (inset of Fig. 4-a) depicts the average crystallite size of Ag NPs (black spots) which were approximately 20 nm. Fig. 4-b shows the high resolution TEM (HRTEM) images of the HGCA0.8 sample, confirming the existence of Ag NPs (dark spots) through their corresponding inverse fast Fourier transform (IFFT) pattern and the lattice fringe profile (LFP). The detected reflection from the (0 0 2) lattice plane of Ag was well matched to the ICDD card number 01-071-5025 for bulk Ag crystal.

Fig. 5 displays the EDX elemental maps of the HGCA0.8 nanocomposite. The homogeneous distribution of the detected constituent elements (such as holmium, oxygen, phosphorous, boron, zinc, and sulfur) was clearly evidenced. Moreover, the presence of Ag (as white blobs) and the absence of Cl in the studied nanocomposite confirmed the nucleation of Ag NPs from AgCl which was supported by the TEM

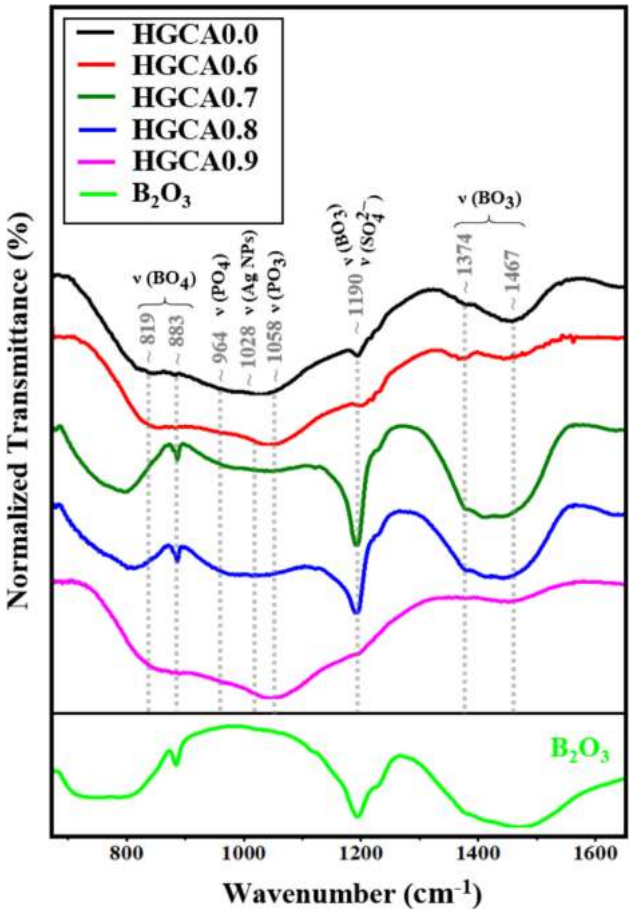

Fig. 3. The FTIR spectra of the prepared glass-ceramic nanocomposites.

and HRTEM results. The formation of Ag NPs in the nanocomposite matrix was attributed to the thermal agitation enabled oxidation-reduction (redox) mechanism during the melting process at high temperature. In this process, the AgCl was completely dissociated at approximately 455 °C to form Ag^+ and Cl^- ions. Then, at around 500 °C all the Cl^- ions were transformed into chlorine gas and then evaporated. Meanwhile, due to the thermal reduction process each Ag^+ gained an electron to form a neutral Ag species. Eventually, few neutral Ag atoms were agglomerated via the mechanism of Ostwald ripening to produce Ag NPs [26].

Complex impedance analysis

Fig. 6-a shows the room temperature Nyquist plot in the frequency range of 1–100 kHz for the HGCA0.0, HGCA0.6 and HGCA0.8 glass-ceramics. The observed single semicircle indicated either the contribution of a single-relaxation process or many relaxation mechanisms in the impedance response with similar relaxation time which caused an overlapping of more than one semicircle. The centres of those semicircles were under the x-axis which presented a non-Debye kind of relaxation mechanism. The collected experimental data were fitted by the ZMAN software. The best fits were achieved by an equivalent circuit consisted of a series resistance R_s connected to the parallel RQ element (Fig. 6-a). The parameter Rs and R represented the corresponding resistance of the crystalline and glassy phase in the glass-ceramic network while Q characterised a constant phase element. The values of the equivalent circuit elements were shown in Table 2. The order of magnitude difference in the Rs (kΩ) and R (MΩ) values suggested the dominance of the glass phase in the proposed glass-ceramic nanocomposites. The values of Rs and R in the host network was remarkably affected due to the addition of Ag NPs in which the value of Rs was

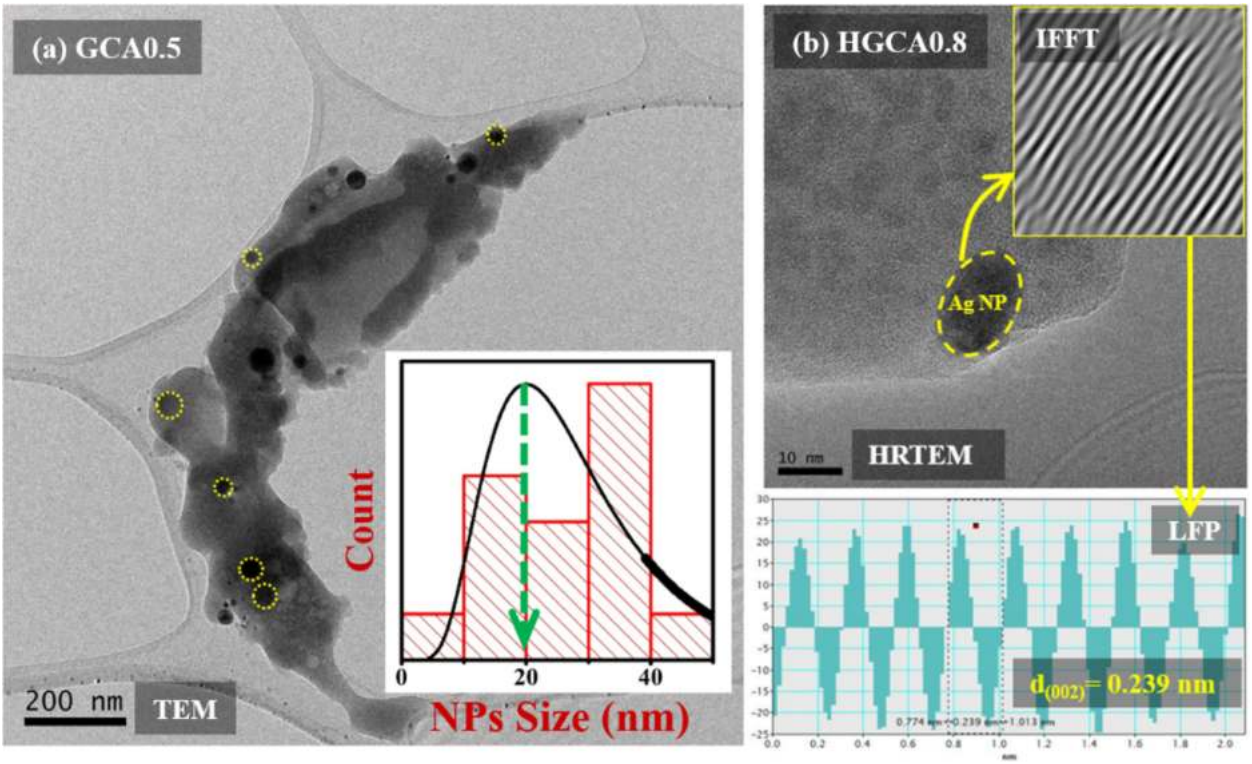

Fig. 4. (a) Low magnification TEM image for GCA0.5 sample (Inset: the mean crystallite size distribution), (b) HRTEM image of the HGCA0.8 sample (Insets: the corresponding IFFT pattern (top) and LFP (bottom)).

decreased while R was increased, indicating the structural alterations around the Ho^{3+}. The observed improvement in the Rs value (from 455–511 Ω) and R value (from 2.01–2.53 MΩ) with the increase of the Ag NPs from 0.6–0.8 mol% was suggested the enhancement of the network disordering.

Fig. 6-b displays the frequency dependent AC conductivity (σ_{Ac}) of the HGCA0.0, HGCA0.6 and HGCA0.8 nanocomposites calculated as stated in [27]. Generally, the conductivity of such system mainly depends on two factors including the (i) concentration of the transition-metal ions (Zn in the present compositions) and (ii) dopant-induced structural modifications. In other words, the addition of Ag NPs in the host matrix reduced the number of ions present inside the network structure, resulting in a slight decrease in the σ_{Ac} value.

Fig. 6-c and d demonstrate the influence of Ag NPs inclusion on the frequency-dependent dielectric constant (ε′) and dielectric loss (ε″) response (estimated as reported in [28,29]). The initial behaviour of ε′ was mainly ascribed to the space charge polarisation effect [30]. At higher frequencies, the values of ε′ for the HGCA0.0 nanocomposite exhibited a decreasing tendency and an increasing trend for the HGCA0.6 and HGCA0.8 glass-ceramics. This observation for the HGCA0.0 nanocomposite was essentially assigned to the low probability of the molecular dipoles to produce a strong polarisation (which needed more time to reorient in the existence of an external applied field) [31]. However, for the nanocomposites prepared with 0.6 and 0.8 mol% of the Ag NPs reasonably strong polarisation was developed from the surface plasmon polariton field of the Ag NPs. Conversely, the value of ε″ was initially dropped with the increase in the externally applied frequency and then either slightly increased (for the HGCA0.0 nanocomposite) or decreased (for HGCA0.6 and HGCA0.8 nanocomposites). The observed reduction at lower frequencies was ascribed

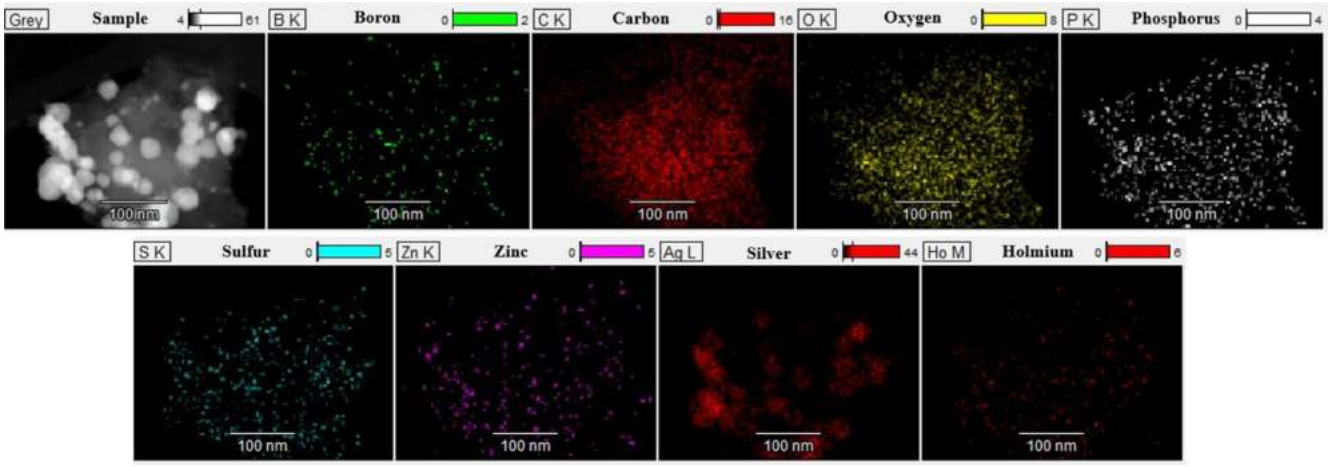

Fig. 5. The EDX elemental maps of the HGCA0.8 nanocomposite.

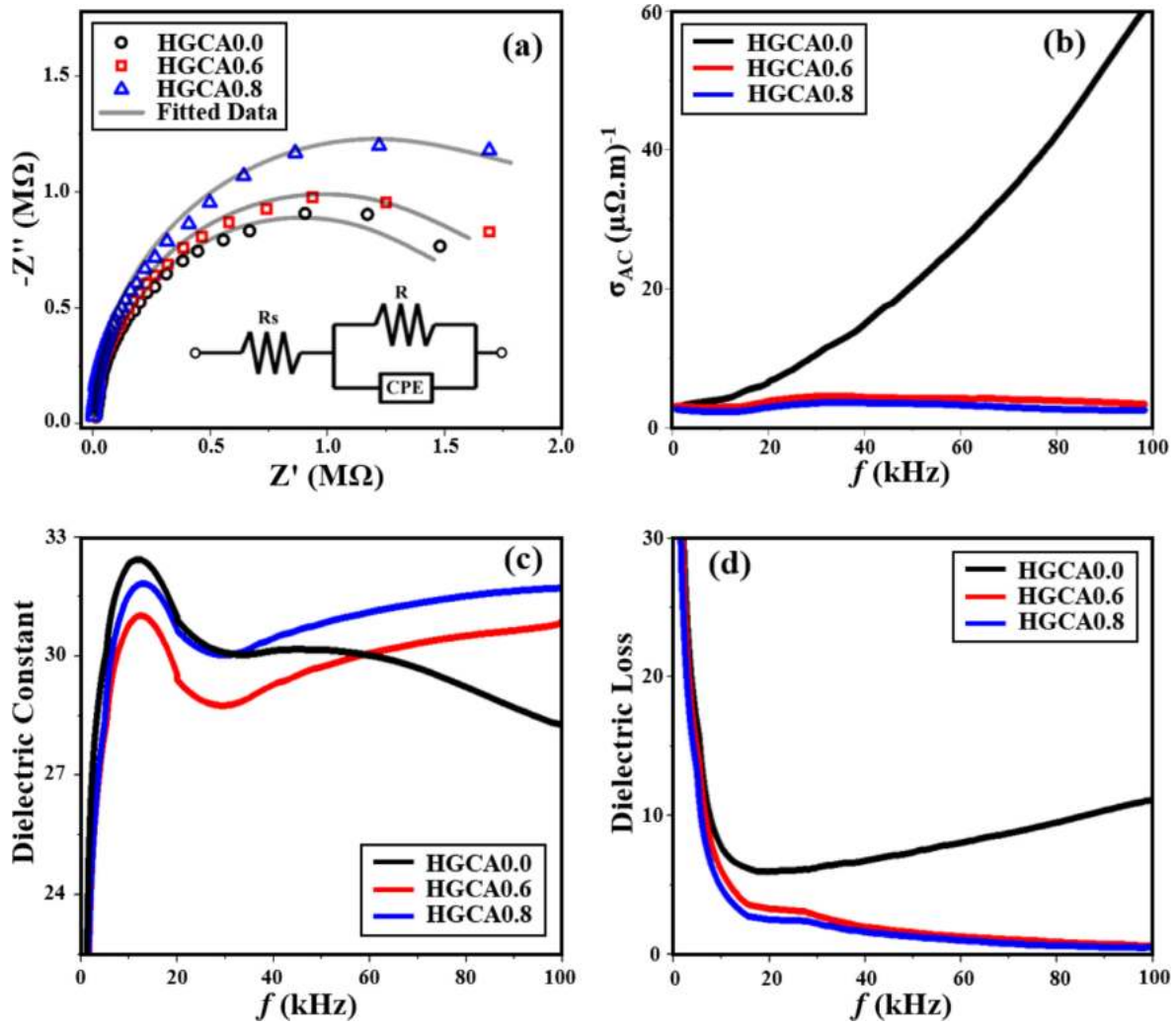

Fig. 6. The impedance and dielectric response of the HGCA0.0, HGCA0.6 and HGCA0.8 glass-ceramic nanocomposites (a) the Nyquist plots, (b) the frequency-dependent σ_{Ac}, (c) ε' and (d) ε''.

Table 2
The values of the equivalent circuit elements obtained using the ZMAN software.

Sample	Rs (kΩ)	R (MΩ)	*CPE*	
			Q (pF)	n
HGCA0.0	11.35	1.85	49.88	0.98
HGCA0.6	0.455	2.01	48.29	0.99
HGCA0.8	0.511	2.53	47.49	1

to the relaxation of the dipoles and their orientations where the hopping of the charge carriers followed the changes in the externally applied frequency [32,33].

Optical properties

Absorption spectral analysis

Fig. 7 displays the recorded transmission and reflectance data for the HGCA0.8 sample. The inset of Fig. 7 shows the physical appearance of the obtained transparent glass-ceramic. Fig. 8-a and b show the absorption spectra (obtained from the optical reflectance and transmittance [34]) of the as-quenched HGCA0.8 glass-ceramic nanocomposite in the visible and NIR regions. It consisted of thirteen peaks that corresponded to various electronic transitions from the ground state ($^5I_8$)

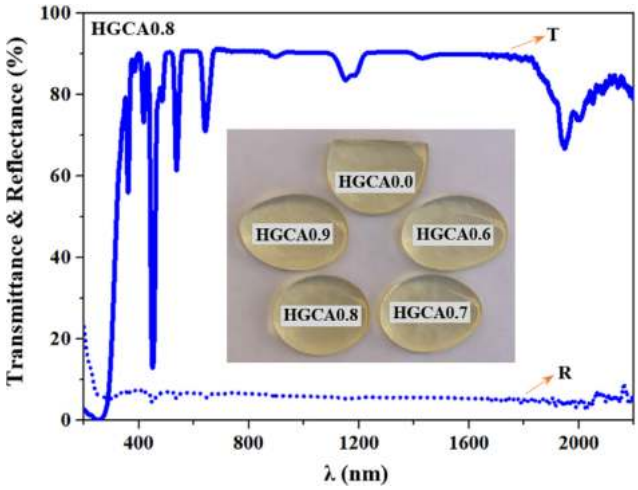

Fig. 7. The transmittance (line spectra) and reflectance (dots spectra) of the HGCA0.8 nanocomposite. Inset: the physical appearance of the actual samples under sunlight.

to the upper excited states ($^5I_7$, $^5I_6$, $^5I_5$, $^5F_5$, $^5F_4$, $^5F_3$, $^3K_8$, $^5G_6$, $^5G_5$, $^3K_7$, $^3H_6$, $^3L_9$ and $^3K_6$) of Ho^{3+} [35]. The inset of Fig. 8-b depicts the absorption spectra of the GCA0.5 sample (prepared without Ho^{3+}) which

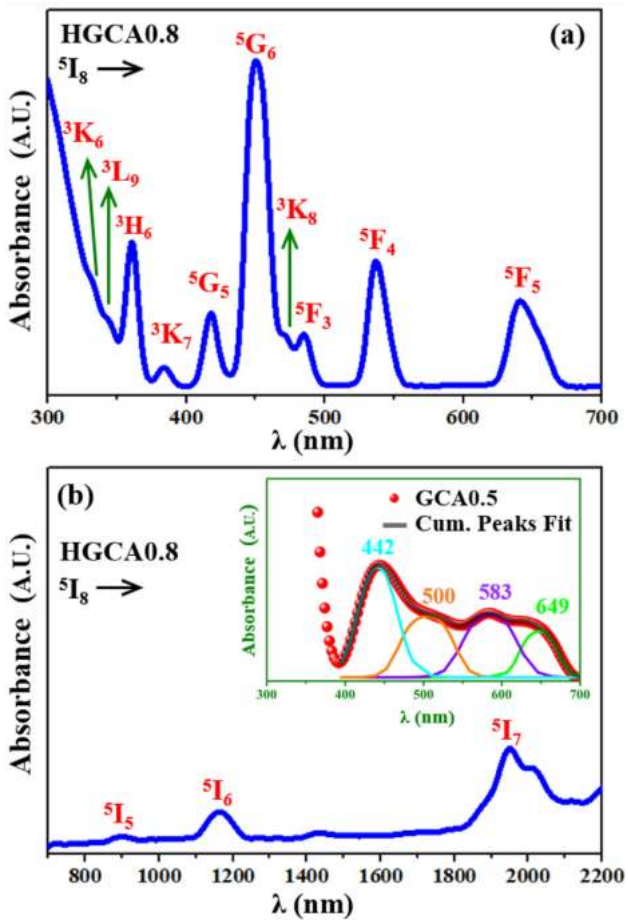

Fig. 8. The absorption spectra of the HGCA0.8 nanocomposite in the (a) visible and (b) IR region (Inset: LSPR bands of the Ag NPs existed in the GCA0.5 nanocomposite prepared without Ho^{3+} that was fitted to the Gaussian-Lorentzian cross function).

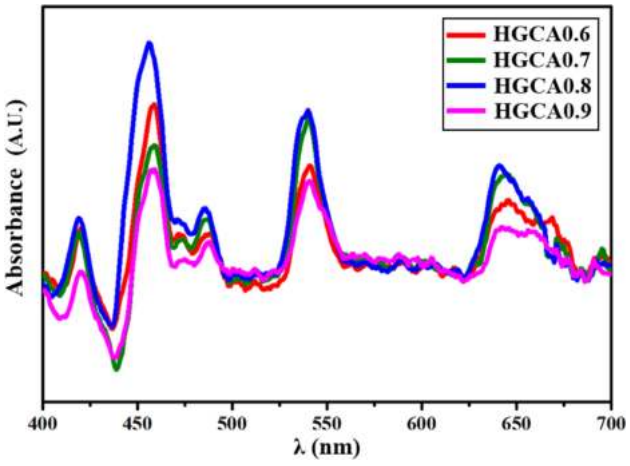

Fig. 9. The absorption spectra of the studied nanocomposites after subtracted from the HGCA0.0 sample contribution.

was deconvoluted to identify the presence of Ag NPs LSPR bands in the current glass-ceramic. The observed four bands were attributed to the following factors: (i) varying shapes of Ag NPs; (ii) the presence of multiple resonance modes (such as the dipole, quadrupolar, octupole and hexadecapole mode); (iii) the coupling of two independent resonators (two NPs) with anti-symmetric shapes that caused some splitting of the dipole modes into transverse and longitudinal types

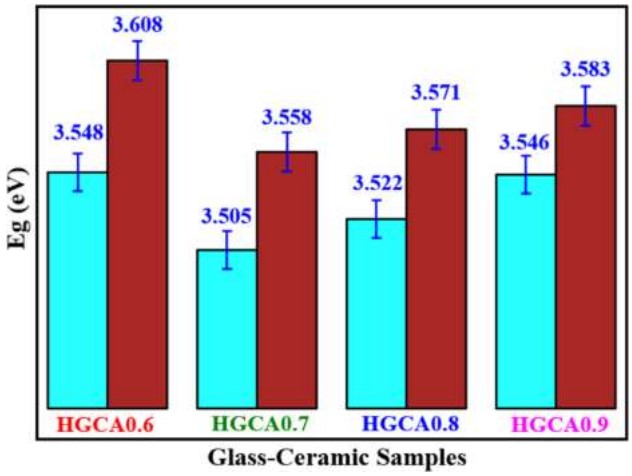

Fig. 10. The optical band gap energies of the studied 4 nanocomposites (cyan colour: Tauc' method and maroon color: ASF' method). (For interpretation of the references to color in this figure legend, the reader is referred to the web version of this article.)

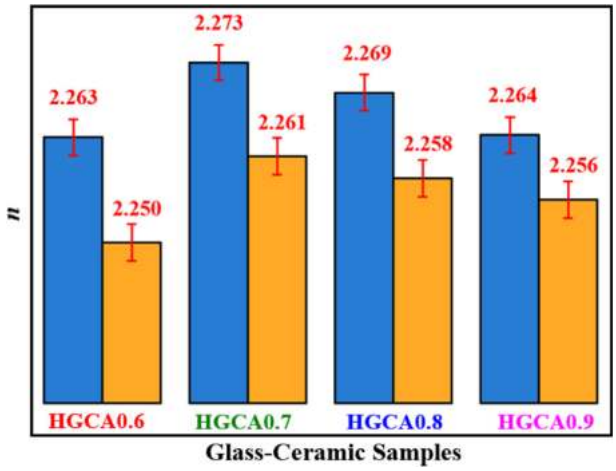

Fig. 11. The refractive indices of the 4 glass-ceramics determined from the values of E_g (Tauc' E_g: blue columns. ASF' E_g: yellow columns). (For interpretation of the references to color in this figure legend, the reader is referred to the web version of this article.)

responsible for the hybridized states and the formation of the new states [36–40]. To determine the effect of the Ag NPs LSPR modes on the absorption features of the proposed glass-ceramic nanocomposites, the absorption spectra of the HGCA0.6, HGCA0.7, HGCA0.8, and HGCA0.9 samples were subtracted from that of the HGCA0.0 sample (prepared without Ag NPs). Fig. 9 shows the resultant spectra, suggesting the manifestation of the strongest LSPR modes by the HGCA0.8 nanocomposite. In addition, the absorption spectra (Fig. 8) for all samples were analysed to determine the optical band gap energy and Judd-Ofelt intensity parameters.

Optical band gap, refractive index, and urbach energy

For accurate evaluation of the optical band gap energy (E_g) for the proposed glass-ceramics, two methods were used such as the (i) Tauc plot and (ii) absorption spectrum fitting (ASF) which is independent of the sample thickness. The Tauc plot involved the $(\alpha h\nu)^{1/r}$ against photon energy ($h\nu$). Conversely, the ASF method first estimated the wavelength (λ_g) corresponding to the optical band gap energy ($E_g = hc/\lambda_g$) from the plot of $(A\lambda^{-1})^m$ against λ^{-1} (where the index m takes the value 2 and 0.5 depending on the direct and indirect allowed optical transitions across the band gap, respectively) and then

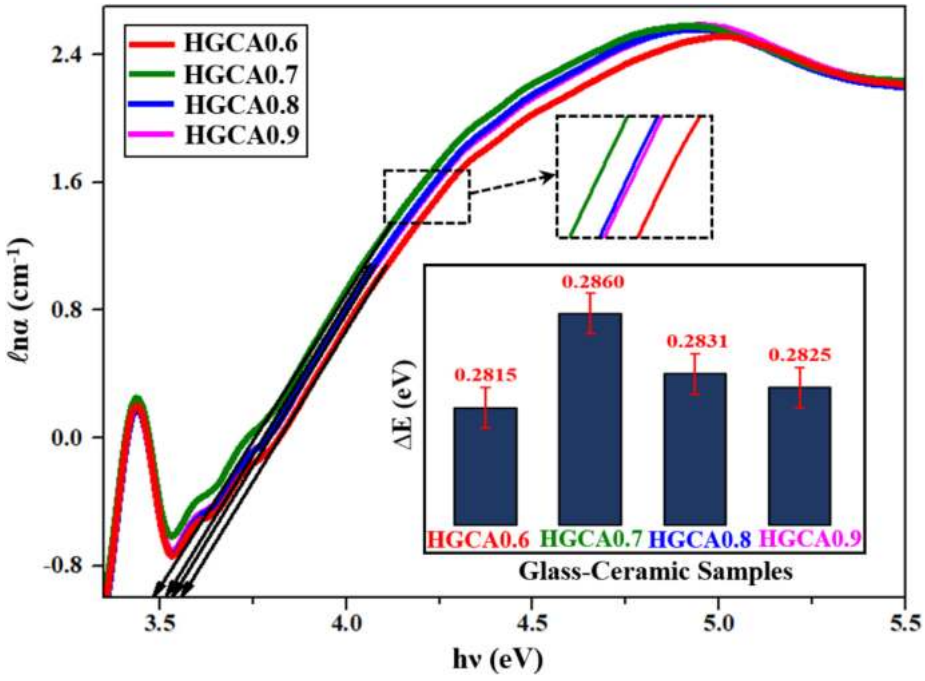

Fig. 12. The determination of the Urbach energy of the prepared of the prepared nanocomposites (Inset: Ag NPs content dependent Urbach energy).

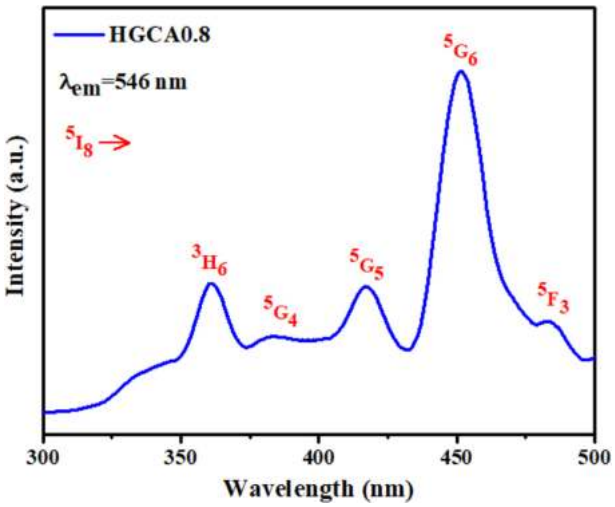

Fig. 13. The PL excitation spectra of the HGCA0.8 nanocomposite.

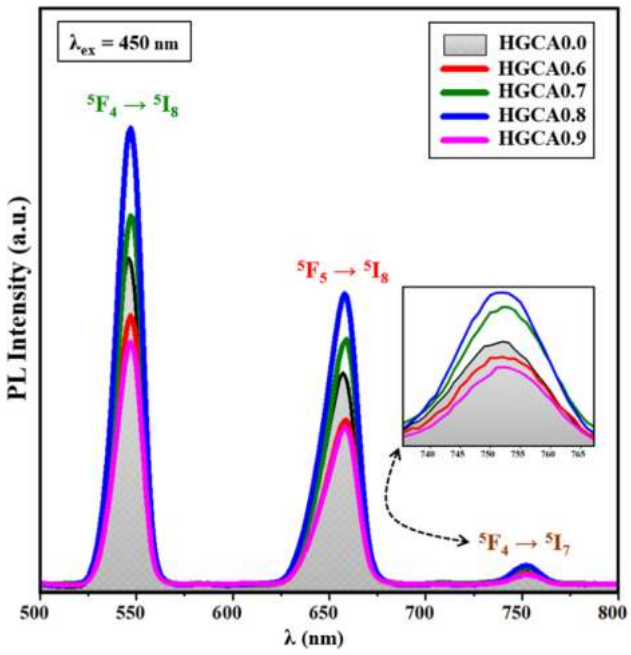

Fig. 14. The PL emission spectra of the prepared glass-ceramics.

calculated the value of E_g [41]. The indirect E_g values for all nanocomposites containing both Ho^{3+} and Ag NPs were presented in Fig. 10. The observed variation in the E_g values (from 3.505 to 3.608 eV) with the increasing Ag NPs contents was ascribed to the emergence of the extra localized energy states in the optical band gap [42]. The values of *n* were determined from the values of E_g (Dimitrov and Sakka relation [43]) and depicted in Fig. 11. The observed behavior of *n* can be correlated to the density (ρ) of the prepared glass-ceramics to define a structural-optical interrelationship. Such correlation is useful to achieve the optimum conditions for the Ho^{3+} PL emission enhancement in the proposed nanocomposites controlled by the Ag NPs contents. The lower value of ρ (the larger the molar volume) indicated an easy distortion of the electron cloud associated to the network units and thus resulted in the higher polarizability of the nanocomposites. Consequently, such distortion was responsible for the generation of dispersion forces and hence the higher dispersion. This higher dispersion caused the more bending or refraction of light in the material (slowed down the light propagation) and thus producing higher *n*.

Fig. 12 shows the variation of ΔE (obtained by Urbach expression [44]) values of the studied nanocomposites as a function of Ag NPs concentration. The higher Urbach energy indicated a higher disorder in the host nanocomposite matrix. The reason for such disorder in the current glass-ceramic nanocomposites can be attributed to the impurities and vacancies contributed more localized states inside the optical band gap, displaying an inverse correlation between the ΔE and Eg values [45,46]. The trend of ΔE (ranged from 0.281 to 0.286 eV) variation in the proposed glass-ceramics was somewhat analogous to the behavior of *n* values fluctuation (higher disorder caused more bending of light inside the networks of nanocomposites). Also, the trend of ΔE (enhancement of the network disordering) with the rise of Ag NPs contents from 0.6 to 0.8 mol% supported by the IS analysis. Based on

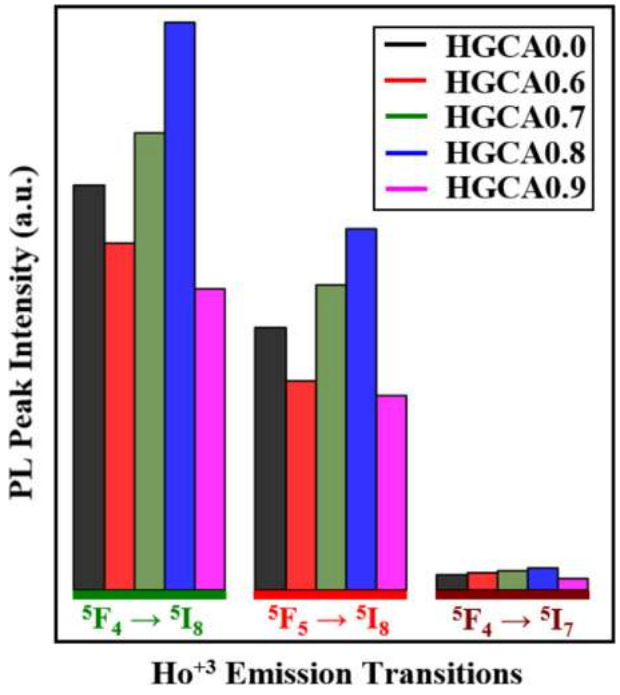

Fig. 15. The PL peak intensity against Ho^{3+} emission transitions of the nanocomposites.

these revelations, a structural, optical and dielectric relationship in the prepared glass-ceramic nanocomposites can be established.

Photoluminescence excitation and emission spectral analysis

Fig. 13 displays the PL excitation spectra of the HGCA0.8 sample tracked at the emission wavelength of 546 nm (the position of the most intense absorption peak). The excitation spectra of the proposed glass-ceramic system revealed 5 significant peaks at approximately 360, 384, 413, 450 and 485 nm corresponding to the transitions from the ground state ($^5I_8$) to the excited states $^3H_6$, $^5G_4$, $^5G_5$, $^5G_6$ and $^5F_3$ in Ho^{3+} [34,47]. The wavelength of the observed most intense excitation peak (~450 nm) was used to record the PL emission spectra for the prepared glass-ceramics for evaluation of the optical properties. Fig. 14 displays the PL spectra of the produced glass-ceramic nanocomposites obtained with 450 nm excitation wavelength. The observed 3 significant PL peaks were assigned to the IR ($^5F_4 \rightarrow {}^5I_7$), red ($^5F_5 \rightarrow {}^5I_8$) and green ($^5F_4 \rightarrow {}^5I_8$) emissions of Ho^{3+}. These peaks were well matched with the reported literature findings [8,47]. The intensity of the green emission ($^5F_4 \rightarrow {}^5I_8$) was the highest. Also, all the peak intensities were first enhanced with the increase in the Ag NPs contents up to 0.8 mol% (Fig. 15) and then quenched at 0.9 mol%. This quenching in the PL intensity was due to the energy transfer process between the neighboring Ho^{3+} as well as between the metal NPs and Ho^{3+}. The PL intensity enhancement was mainly ascribed to the LSPR mediated effect of the Ag NPs where a strong electric field was generated around the Ho^{3+} positioned in the proximity of the NPs inside the glass-ceramic matrix [48,49]. This LSPR field amplified both the local incident electromagnetic field (also called local field enhancement or LFE in short) that led to the increment in the excitation rate due to the resonant coupling with the LSPR modes (442 nm in the current case) as well as the emission rate where the LSPR wavelength overlapped with the emission wavelength. The ET from the Ag NPs to Ho^{3+} occurred due to the resonance effects between the Ag NPs absorption bands and excited levels of the Ho^{3+} [50]. In this mechanism, the presence specific electronic states of the Ag NPs can transfer the energy to the Ho^{3+} not in the form of luminescence [51]. Fig. 16 shows schematically the detected absorption bands of the Ho^{3+} and Ag NPs (LSPR modes) inside the host matrix in the presence of various mechanisms including the ET,

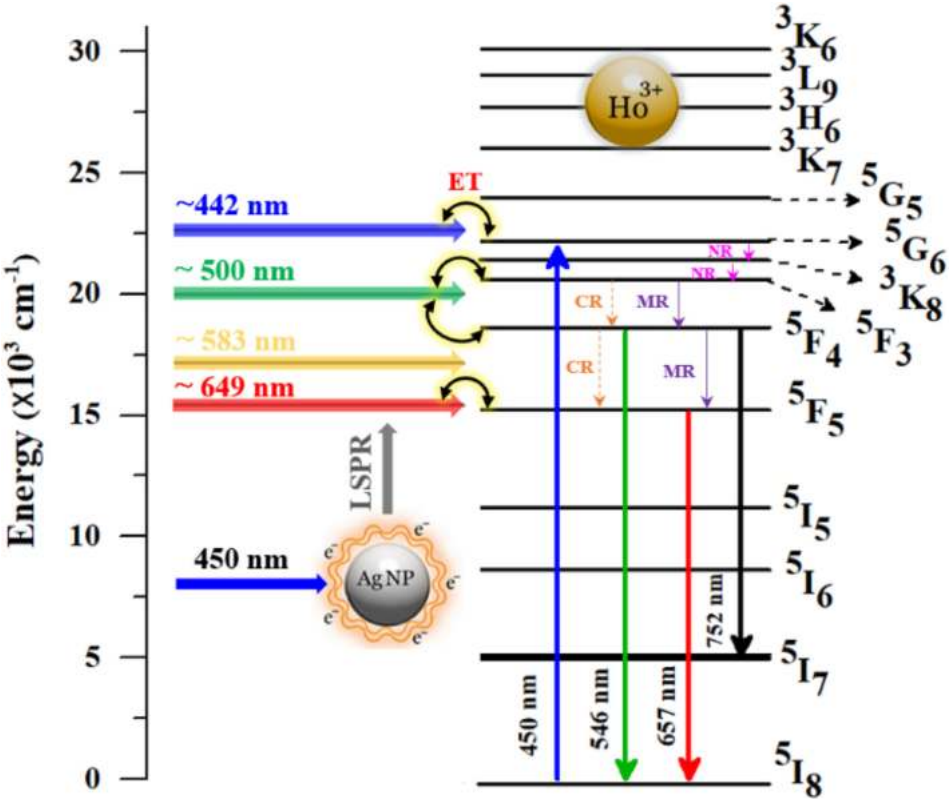

Fig. 16. The energy level scheme of the Ho^{3+} depicting the excitation, emission and some possible energy transfer mechanisms of the Ho^{3+} positioned in the proximity of the Ag NPs inside the host network. NR: non-radiative transitions; MR: multi-phonon relaxations; CR: cross relaxations.

Table 3
Experimental (f_{exp} $\times 10^{-6}$) and calculated (f_{cal} $\times 10^{-6}$) oscillator strength and the root-mean-square deviation (δ_{rms}) of the synthesized glass samples.

Transition	HGCA0.6		HGCA0.7		HGCA0.8		HGCA0.9	
	f_{exp}	f_{cal}	f_{exp}	f_{cal}	f_{exp}	f_{cal}	f_{exp}	f_{cal}
$^5I_8 \rightarrow {}^5I_7$	5.995	6.817	6.322	7.173	6.023	6.872	6.112	6.835
$^5I_8 \rightarrow {}^5I_6$	3.977	4.477	4.346	4.748	4.078	4.526	3.820	4.507
$^5I_8 \rightarrow {}^5I_5$	0.964	0.814	0.928	0.874	0.686	0.835	1.093	0.829
$^5I_8 \rightarrow {}^5F_5$	13.21	12.86	14.16	13.66	13.46	13.12	12.94	12.80
$^5I_8 \rightarrow {}^5F_4$	17.61	13.48	18.78	14.31	18.12	13.70	17.62	13.49
$^5I_8 \rightarrow {}^5F_3$	2.154	4.785	1.462	5.075	2.001	4.829	1.763	4.827
$^5I_8 \rightarrow {}^3K_8$	0.167	3.680	0.231	3.882	0.131	3.731	0.114	3.693
$^5I_8 \rightarrow {}^5G_6$	61.97	63.16	65.26	66.49	63.27	64.52	62.22	63.41
$^5I_8 \rightarrow {}^5G_5$	10.81	13.28	11.31	14.14	11.14	13.72	10.84	13.11
$^5I_8 \rightarrow {}^3K_7$	2.350	0.909	2.468	0.961	2.484	0.921	2.605	0.914
$^5I_8 \rightarrow {}^3H_6$	21.50	10.80	22.38	11.37	22.22	11.01	21.47	10.82
$^5I_8 \rightarrow {}^3L_9$	0.613	3.813	0.835	4.036	0.576	3.855	0.674	3.843
$^5I_8 \rightarrow {}^3K_6$	0.699	0.155	1.889	0.163	0.984	0.157	1.089	0.156
δ_{rms}	3.638 $\times$ 10^{-6}		3.862 $\times$ 10^{-6}		3.816 $\times$ 10^{-6}		3.661 $\times$ 10^{-6}	

Table 4
The J-O parameters ($\times 10^{-20}$ cm^2) and the spectroscopic quality factor (χ) of the studied glass-ceramics.

Sample	Ho^{3+} (mol%)	Ω_2	Ω_4	Ω_6	χ
HGCA0.6	0.5	7.75	6.54	4.23	1.547
HGCA0.7	0.5	8.05	6.91	4.45	1.553
HGCA0.8	0.5	7.82	6.71	4.25	1.581
HGCA0.9	0.5	7.81	6.44	4.26	1.511
Ref. [34]	0.5	12.7	10.5	6.42	1.63
Ref. [47]	0.5	4.33	5.28	2.27	2.32
Ref. [8]	0.5	8.05	2.77	2.31	1.20

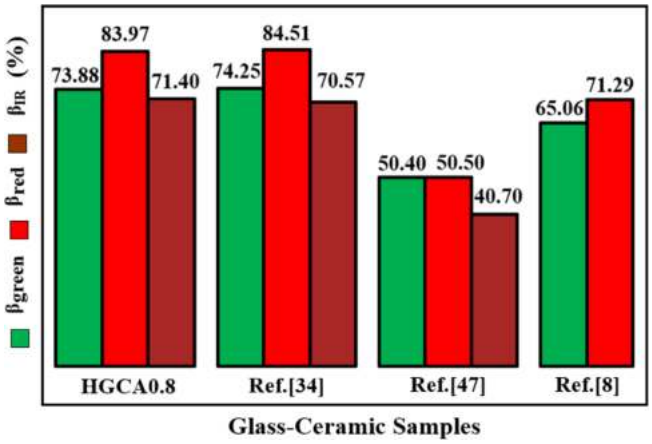

Fig. 17. The values of β_R (%) for the three PL emissions of the HGCA0.8 nanocomposite when compared with other reports.

cross-relaxation, multi-phonon relaxations, non-radiative and radiate decays. These Ag NPs acted as the sensitizers where upon the excitation via the appropriate wavelength (450 nm in the present case), the energy was transferred to the Ho^{3+} and consequently triggered the occupation of their excited states before decayed radiatively by the emission (PL) of light [52]. Meanwhile, some excited states decayed non-radiatively due to the existence of many closed lying energy levels in the Ho^{3+}. In the present work, the HGCA0.8 nanocomposite that revealed the optimum PL enhancement also exhibited the highest LSPR band intensity as predicted by the absorption spectral analysis (Fig. 9). This finding indicated the most favourable nature of the proposed host matrix as well as the best doping concentration of the Ag NPs (0.8 mol%) for efficient synergism, enabling a simultaneous enhancement in the PL intensity towards an intense green and red lasing actions.

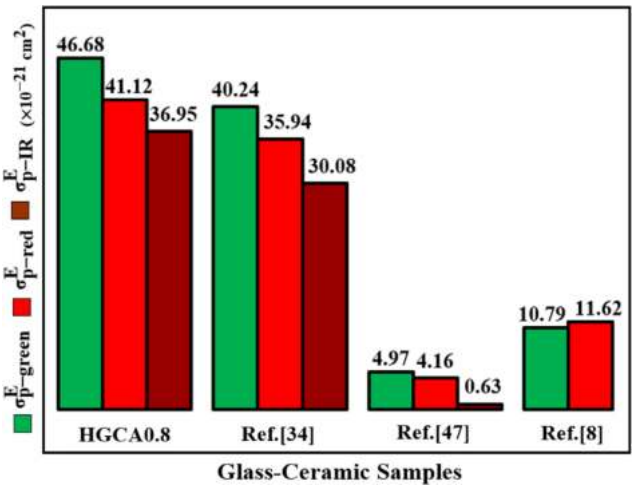

Fig. 18. The values of $\sigma_p^E \cdot (\times 10^{-21} cm^2)$ for the three PL emissions of the HGCA0.8 glass-ceramic compared to other reported works.

J-O intensity and radiative parameters

Following the earlier work [34], the J-O intensity parameters (Ω_2, Ω_4, and Ω_6) of the prepared glass-ceramic nanocomposites were calculated. The J-O evaluation was performed using the values of the refractive indices together with the matrix elements and the oscillator strengths of the recorded transitions in the Ho^{3+} 4f quantum states. Table 3 shows the values of the experimental and calculated oscillator strengths of the proposed nanocomposites for various transitions in the Ho^{3+} together with their root mean square deviation (δ_{rms}). The observed variation of the oscillator strengths with the increase in the Ag NPs contents was attributed to the higher local symmetry of the host network [53]. The δ_{rms} values were found to be comparable to the other literature reports [8,47,54,55]. Table 4 enlists the calculated J-O intensity parameters which revealed a trend of $\Omega_2 > \Omega_4 > \Omega_6$. In addition, the spectroscopic quality factor (χ) of the glass-ceramics was compared with other reported values. The parameter Ω_2 described the symmetric surrounding the Ho^{3+} and the ligand polarizability produced by the overlap of the orbital ligand and Ho^{3+} [56]. The HGCA0.7 nanocomposite having the largest value of Ω_2 displayed the lowest symmetric environment around the Ho^{3+}, indicating the stronger polarizability. The values of Ω_2 were varied from 7.75 to 8.08 ($\times 10^{-20}$cm^2) with the rise in the Ag NPs concentration from 0.6 to 0.9 mol%. This variation was consistent with the change in the V_m, n, and ΔE values, confirming the exposed structural-optical relationship in the present nanocomposites. The parameters Ω_6 and Ω_4 signified the

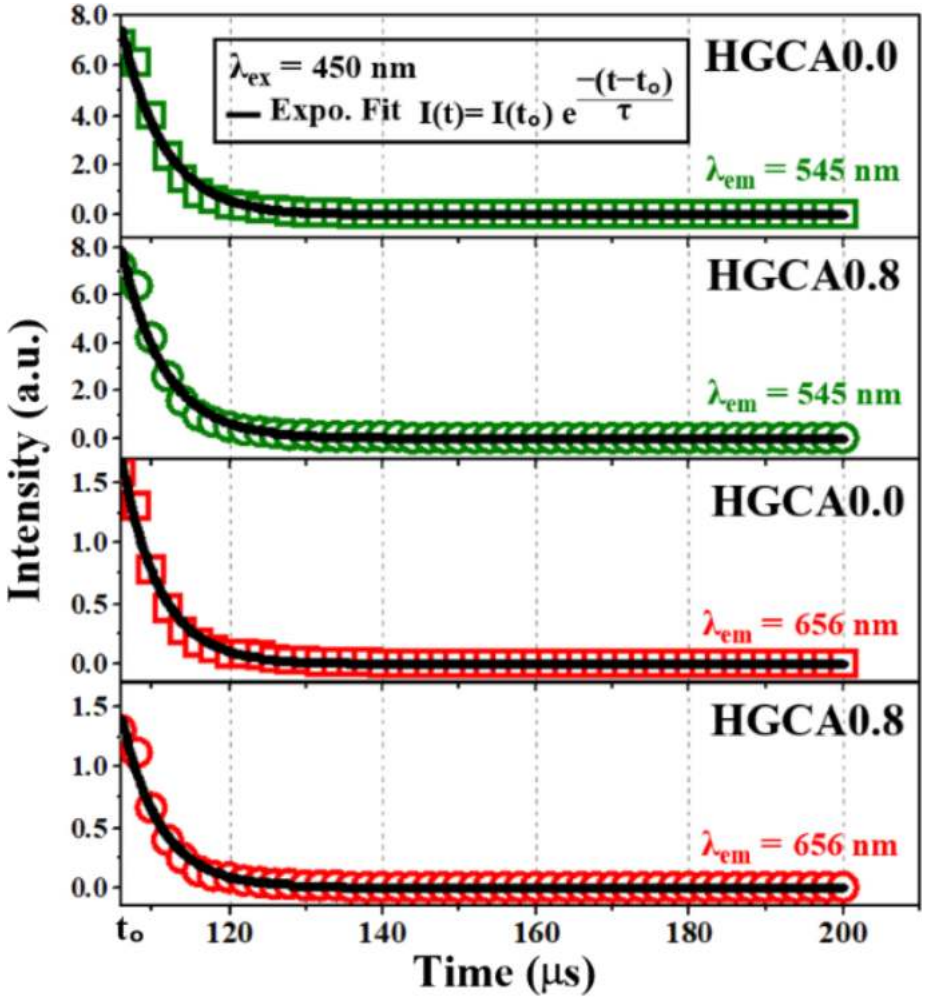

Fig. 19. Measured luminescence decay curve at 545 nm ($^5F_4 \rightarrow {}^5I_8$) and 656 nm ($^5F_5 \rightarrow {}^5I_8$) for HO^{3+}.

Table 5
Measured lifetimes, radiative lifetimes, non-radiative decay rate and quantum efficiencies of Ho^{3+} in the HGCA0.0 and HGCA0.8 nanocomposites.

Sample	$^5F_4 \rightarrow {}^5I_8$ (green)				$^5F_5 \rightarrow {}^5I_8$ (red)			
	τ_{mes} (μs)	τ_{rad} (μs)	W_{NR} (μs^{-1})	η (%)	τ_{mes} (μs)	τ_{rad} (μs)	W_{NR} (μs^{-1})	η (%)
HGCA0.0	5.52	49.27	0.16	11.20	4.97	101.26	0.19	4.91
HGCA0.8	5.56	24.06	0.14	23.11	5.03	49.72	0.18	10.12
Ref. [64]	7.65	65	–	11	–	–	–	–
Ref. [65]	2.13	–	–	–	–	–	–	–

dielectric properties, rigidity and the viscosity of the host matrix [56,57]. The obtained behavior of the network rigidity (related to ρ and V_m values) revealed by the change in the Ω_4 value [58,59]. Moreover, the lasing potency of the Ho^{3+} in the titled glass-ceramics can be justified by the values of χ, wherein the nanocomposite with large χ value is established to be a viable candidate for the solid state laser development [11]. In this study, the HGCA0.8 nanocomposite disclosed the highest χ value which was further supported by the results on the PL intensity enhancement.

Fig. 17 compares the fluorescence branching ratio (β_R) of the HGCA0.8 glass-ceramic obtained for all the detected PL peaks with the existing literature on other hosts containing 0.5 mol% of Ho^{3+}. It is known that a solid state system with β_R value above 50% can offer the potent lasing actions [60], wherein the parameter β_R describes the probability of the stimulated emission transition between two specific energy states obeying the selection rules [61,62]. The achieved values of β_R for the HGCA0.8 nanocomposite were 73.88%, 83.97% and 71.40% for the green ($^5F_4 \rightarrow {}^5I_8$), red ($^5F_5 \rightarrow {}^5I_8$) and IR ($^5F_4 \rightarrow {}^5I_7$) emissions, respectively. In short, these large values of β_R clearly indicated the effectiveness of the produced glass-ceramic nanocomposites for the construction of red and green lasers.

Fig. 18 presents the stimulated emission cross-section (σ_P^E in cm^2) of all the recorded PL emissions for the HGCA0.8 nanocomposite and compares them with the existing literature on other hosts containing 0.5 mol% of Ho^{3+}. The value of σ_P^E implies the capacity of the photons emission from a specimen that can be an efficient lasing media [61], where large σ_P^E values are favorable for the low threshold and high gain laser fabrication [60]. The achieved larger values of σ_P^E for the HGCA0.8 nanocomposite (46.68×10^{-21} cm^2, 41.12×10^{-21} cm^2 and 36.95×10^{-21} cm^2 for the green ($^5F_4 \rightarrow {}^5I_8$), red ($^5F_5 \rightarrow {}^5I_8$) and IR ($^5F_4 \rightarrow {}^5I_7$) emissions, respectively) nominated its composition for the fabrication of intense green and red laser devices. Based on the present

findings, it can be affirmed that the observed alteration in the spectroscopic traits of the proposed nanocomposites was indeed induced by their structural modifications (such as the symmetry, ligand interaction, and LSPR of Ag NPs).

PL decay rates and quantum efficiency

Fig. 19 displays the luminescence decay curve measured at 545 nm ($^5F_4 \rightarrow {}^5I_8$) and 656 nm ($^5F_5 \rightarrow {}^5I_8$) for the HGCA0.0 and HGCA0.8 nanocomposites. The experimental lifetime (τ_{mes}) of the excited levels ($^5F_4$ and $^5F_5$) were obtained by the exponential fit of the measured curves (Table 5). The values of the radiative lifetimes (τ_{rad}, calculated from the J-O theory), the non-radiative decay rate (W_{NR}) and quantum efficiency (η) (estimated following [63]) of the Ho^{3+} doped inside the HGCA0.0 and HGCA0.8 nanocomposites are also presented in Table 5. The obtained very low η values (comparable with other reports) were primarily ascribed to the closeness of several excited energy levels in Ho^{3+}. The observed increase in the τ_{mes} values was mainly attributed to the Ag NPs LSPR mediated enhanced local electric field effect and the energy transfer from the Ag NPs to the Ho^{3+} [63]. The values of the experimental radiative lifetime were found to be shorter than the calculated ones which may be due to the nonradiative relaxation of the excited state of the Ho^{3+} in the proposed host [63]. According to the literature, the quantum efficiency of a particular emission transition is strongly influenced by some factors such as the emission cross-section, radiative transition probability, lifetime of the metastable state, REI concentration and ligand field effects [5]. In the present disclosure, the green emission from the HGCA0.8 nanocomposite showed the highest quantum efficiency and lowest non-radiative decay rate, thereby indicating its promise as the green lasing media.

Conclusions

The Ho^{3+}-activated (fixed content) and Ag NPs (varying contents) sensitized five zinc-sulfo-boro-phosphate glass-ceramic nanocomposites were prepared via the standard melt-quenching. The as-quenched nanocomposites were characterised to evaluate their structural, optical and dielectric traits as a function of various Ag NPs concentrations. The J-O theoretical calculations were conducted to complement the experimental data. A correlation was established for the first time among the observed variation in the Ag NPs concentration dependent values of ρ, V_m, Eg, n, ΔE, σ_{Ac} and J-O parameters (intensity and radiative). It was demonstrated that the synergism between the inserted Ho^{3+} and Ag NPs inside the proposed glass-ceramic nanocomposites can be effective to customize their spectroscopic attributes, especially the PL emission characteristics required for various miniaturized visible light emitting devices. The PL peak intensity enhancement of the current nanocomposite prepared with 0.8 mol% of Ag NPs was highest compared to those reported for other Ho^{3+} (0.5 mol%) doped hosts. This disclosure was mainly attributed to the Ag NPs LSPR mediated effect where a strong electric field was generated in the Ho^{3+} surrounding that was located in the close vicinity of the NPs inside the glass-ceramic network. In short, the proposed glass-ceramic compositions are asserted to be beneficial for the development of functional composite materials needed for solid-state laser and various optoelectronic devices.

CRediT authorship contribution statement

Areej S. Alqarni: Conceptualization, Methodology, Investigation, Resources, Writing - original draft. **R. Hussin:** Conceptualization, Supervision. **S.N. Alamri:** Conceptualization, Supervision. **S.K. Ghoshal:** Conceptualization, Supervision, Writing - review & editing.

Declaration of Competing Interest

The authors declare that they have no known competing financial interests or personal relationships that could have appeared to influence the work reported in this paper.

Acknowledgements

We would like to thank the financial and technical assistance from Taibah University, UTM, and the research grant KPT/FRGS/MoHE Vot. 5F050 and UTMFR 20H65.

References

[1] Morassuti CY, Andrade LHC, Silva JR, Baesso ML, Guimarães FB, Rohling JH, et al. J Lumin 2019;210:376–82. https://doi.org/10.1016/j.jlumin.2019.02.051.
[2] Li B, Liang J, Sun L, Wang S, Sun Q, Devakumar B, et al. J Lumin 2019;211:388–93. https://doi.org/10.1016/j.jlumin.2019.04.001.
[3] B. Henderson, G.F. Imbusch, Optical Spectroscopy of Inorganic Solids, clarendon press, Oxford, 1989.
[4] Kochanowicz M, Żmojda J, Miluski P, Ragin T, Pisarski WA, Pisarska J, et al. J Alloy Compd 2017;727:1221–6. https://doi.org/10.1016/j.jallcom.2017.08.243.
[5] Mahraz ZAS, Sahar MR, Ghoshal SK. J Alloy Compd 2018;740:617–25. https://doi.org/10.1016/j.jallcom.2017.12.314.
[6] Basavapoornima C, Linganna K, Kesavulu CR, Ju S, Kim BH, Han WT, et al. J Alloy Compd 2017;699:959–68. https://doi.org/10.1016/j.jallcom.2016.12.199.
[7] Pang XG, Eeu TY, Leong PM, Wan Shamsuri WN, Hussin R. Adv Mater Res 2014;895:280–3. https://doi.org/10.4028/www.scientific.net/AMR.895.280.
[8] Jupri SA, Ghoshal SK, Omar MF, Yusof NN. J Alloy Compd 2018;753:446–56. https://doi.org/10.1016/j.jallcom.2018.04.218.
[9] Linganna K, Narro-García R, Desirena H, De la Rosae E, Basavapoornima C, Venkatramu V, et al. J Alloy Compd 2016;684:322–7. https://doi.org/10.1016/j.jallcom.2016.05.082.
[10] Ravi Kumar V, Giridhar G, Sudarsan V, Veeraiah N. J Alloy Compd 2017:668–81. https://doi.org/10.1016/j.jallcom.2016.11.109.
[11] Moustafa SY, Sahar MR, Ghoshal SK. J Alloy Compd 2017;712:781–94. https://doi.org/10.1016/j.jallcom.2017.04.106.
[12] Ahmadi F, Hussin R, Ghoshal SK. J Lumin 2018;204:95–103. https://doi.org/10.1016/j.jlumin.2018.07.033.
[13] Soltani I, Hraiech S, Horchani-Naifer K, Elhouichet H, Férid M. Opt Mater 2015;46:454–60. https://doi.org/10.1016/j.optmat.2015.05.003.
[14] Ahmadi F, Hussin R, Ghoshal SK. J Non-Cryst Solids 2018;499:131–41. https://doi.org/10.1016/j.jnoncrysol.2018.07.011.
[15] Barnes WL, Dereux A, Ebbesen TW. Nature 2003;424:824–30. https://doi.org/10.1038/nature01937.
[16] Johnson PB, Christy RW. Phys L Re View B 1972;6:4370–9.
[17] Alqarni AS, Hussin R, Alamri SN, Ghoshal SK. Ceram Int 2019;46:3282–91. https://doi.org/10.1016/j.ceramint.2019.10.034.
[18] Abouhaswa AS, Rammah YS, Ibrahim SE, El-Hamalawy AA. J Non-Cryst Solids 2018;494:59–65. https://doi.org/10.1016/j.jnoncrysol.2018.04.051.
[19] Barde RV, Nemade KR, Waghuley SA. J Asian Ceram Soc 2015;3:116–22. https://doi.org/10.1016/j.jascer.2014.11.006.
[20] Ashok J, Kostrzewa M, Ingram A, Venkatramaiah N, Srinivasa Reddy M, Ravi Kumar V, Piasecki M, Veeraiah N. J Alloys Compounds 2019;791:278–95. https://doi.org/10.1016/j.jallcom.2019.03.228.
[21] Rao PSG, Siripuram R, Sripada S. Results Phys 2019;13:102–33. https://doi.org/10.1016/j.rinp.2019.02.069.
[22] Wahab FAA, Abdel-baki M. J Non-Cryst Solids 2009;355:2239–49. https://doi.org/10.1016/j.jnoncrysol.2009.07.028.
[23] Sdiri N, Elhouichet H, Ferid M. J Non-Cryst Solids 2014;389:38–45. https://doi.org/10.1016/j.jnoncrysol.2014.01.031.
[24] Bulus I, Dalhatu SA, Hussin R, Wan Shamsuri WN, Yamusa YA. Int J Modern Phys B 2017;31. https://doi.org/10.1142/S0217979217501016.
[25] Yamusa YA, Hussin R, Shamsuri WNW. Indian J Phys 2018;56:932–43. https://doi.org/10.1016/j.cjph.2018.03.025.
[26] Nurhafizah H, Rohani MS, Ghoshal SK. J Non-Cryst Solids 2017;455:62–9. https://doi.org/10.1016/j.jnoncrysol.2016.10.028.
[27] Jlassi I, Sdiri N, Elhouichet H, Ferid M. J Alloy Compd 2015;645:125–30. https://doi.org/10.1016/j.jallcom.2015.05.025.
[28] Alqarni AS, Hussin R, Alamri SN, Ghoshal SK. J Lumin 2020. https://doi.org/10.1016/j.jlumin.2020.117218.
[29] Alqarni AS, Alsobhi BO, Elabbar AA, Yassin OA. Mater Sci Semicond Process 2017;59:18–22. https://doi.org/10.1016/j.mssp.2016.11.033.
[30] Suresh S, Arunseshan C. Appl Nanosci 2014;4:179–84. https://doi.org/10.1007/s13204-012-0186-5.
[31] Zulfiqar Y, Yuan, Iqbal Z, Lu J. Int J Modern Phys B 2017;31:1–11. https://doi.org/10.1142/S0217979217502344.
[32] Sawadh PS, Kulkarni DK. Bull Mater Sci 2001;24:47–50. https://doi.org/10.1007/bf02704839.
[33] James AR, Prakash C, Prasad G. J Phys D Appl Phys 2006;39:1635–41. https://doi.org/10.1088/0022-3727/39/8/024.
[34] Alqarni AS, Hussin R, Ghoshal SK, Alamri SN, Yamusa YA, Jupri SA. J Alloy Compd 2019;808:151706https://doi.org/10.1016/j.jallcom.2019.151706.
[35] Carnall WT, Fields PR, Rajnak K. J Chem Phys 1968;49:4424–42. https://doi.org/10.1063/1.1669893.

[36] M.M. Miller, A.A. Lazarides, 239 (2006), https://doi.org/10.1088/1464-4258/8/4/S26.
[37] Chen K, Adato R, Altug H. ACS Nano 2012;6:7998–8006. https://doi.org/10.1021/nn3026468.
[38] K. Lee, M.A. El-sayed, (2006) 19220–19225, https://doi.org/10.1021/jp062536y.
[39] Kelly KL, Coronado E, Zhao LL, Schatz GC. J Phys Chem B 2003;107:668–77. https://doi.org/10.1021/jp026731y.
[40] Mock JJ, Smith DR, Schultz S. Nano Lett 2003;3:485–91. https://doi.org/10.1021/nl0340475.
[41] Bulus I, Hussin R, Ghoshal SK, Tamuri AR, Jupri SA. Ceram Int 2019. https://doi.org/10.1016/j.ceramint.2019.06.089.
[42] Davis EA, Mott NF. Philos Mag 1970;22:903–22. https://doi.org/10.1080/14786437008221061.
[43] Dimitrov V, Sakka S. J Appl Phys 1996;79:1736–40. https://doi.org/10.1063/1.360962.
[44] Urbach Franz. 1324 1324 Phys Rev 1953;92. https://doi.org/10.1103/physrev.92.1324.
[45] Hager IZ. J Phys Chem Solids 2009;70:210–7. https://doi.org/10.1016/j.jpcs.2008.10.007.
[46] Mott NF, Davis EA. Electronic processes in non-crystalline materials. Oxford: Clarendon Press; 2012.
[47] Venkateswarlu M, Mahamuda S, Swapna K, Prasad MVVKS, Srinivasa Rao A, Shakya S, Mohan Babu A, Vijaya Prakash G. J Luminescence 2015:64–71. https://doi.org/10.1016/j.jlumin.2015.02.052.
[48] Jupri SA, Ghoshal SK, Yusof NN, Omar MF, Hamzah K, Krishnan G. Opt Laser Technol 2020;126:106134https://doi.org/10.1016/j.optlastec.2020.106134.
[49] Awang A, Ghoshal SK, Sahar MR, Arifin R, Nawaz F. J Lumin 2014;149:138–43. https://doi.org/10.1016/j.jlumin.2014.01.027.
[50] A.N.C. Neto, M.A. Couto, R. Reisfeld, Effects of Spherical Metallic Nanoparticle Plasmon on 4f-4f Luminescence: A Theoretical Approach, Elsevier Ltd., 2018, https://doi.org/10.1016/B978-0-08-102378-5.00002-7.
[51] Zhang W, Lin J, Cheng M, Zhang S. J Quant Spectrosc Radiat Transfer 2015;159:39–52. https://doi.org/10.1016/j.jqsrt.2015.03.002.
[52] Eichelbaum BM, Rademann K. Adv Funct Mater 2009;19:2045–52. https://doi.org/10.1002/adfm.200801892.
[53] Said Mahraz ZA, Sahar MR, Ghoshal SK. J Alloys Compounds 2015;649:1102–9. https://doi.org/10.1016/j.jallcom.2015.07.232.
[54] Mahamuda S, Swapna K, Packiyaraj P, Srinivasa Rao A, Vijaya Prakash G. Opt Mater 2013;36:362–71. https://doi.org/10.1016/j.optmat.2013.09.023.
[55] Babu S, Seshadri M, Balakrishna A, Reddy Prasad V, Ratnakaram YC. Physica B: Condensed Matter 2015;479:26–34. https://doi.org/10.1016/j.physb.2015.09.023.
[56] Ahmadi F, Hussin R, Ghoshal SK. J Non-Cryst Solids 2016;448:43–51. https://doi.org/10.1016/j.jnoncrysol.2016.06.040.
[57] Fang Y, Hu L, Liao M, Wen L. Spectrochim Acta – Part A: Mol Biomol Spectrosc 2007;68:542–7. https://doi.org/10.1016/j.saa.2006.12.025.
[58] Jorgensen CK, Reisfeld R. J Less-Common Metals 1983;93:107–12. https://doi.org/10.1016/0022-5088(83)90454-X.
[59] Som T, Karmakar B. Spectrochim Acta Part A Mol Biomol Spectrosc 2011;79:1766–82. https://doi.org/10.1016/j.saa.2011.05.054.
[60] Madhukar Reddy C, Deva Prasad Raju B, John Sushma N, Dhoble NS, Dhoble SJ. Renew Sustain Energy Rev 2015;51:566–84. https://doi.org/10.1016/j.rser.2015.06.025.
[61] Yusof NN, Ghoshal SK, Azlan MN. J Alloy Compd 2017;724:1083–92. https://doi.org/10.1016/j.jallcom.2017.07.102.
[62] Awang A, Ghoshal SK, Sahar MR, Arifin R. Opt Mater 2015;42:495–505. https://doi.org/10.1016/j.optmat.2015.02.009.
[63] Mahraz ZAS, Sahar MR, Ghoshal SK. J Lumin 2017;190:335–43. https://doi.org/10.1016/j.jlumin.2017.05.059.
[64] Damodaraiah S, Lakshmi RPV, Ratnakaram YC. J Mol Struct 2019:127157https://doi.org/10.1016/j.molstruc.2019.127157.
[65] Melato LT, Ntwaeaborwa OM, Kroon RE, Motaung TE, Motloung SV. J Mol Struct 2018. https://doi.org/10.1016/j.molstruc.2018.08.093.